




# Water-window high harmonic generation with 0.8- $\mu\text{m}$ and 2.2- $\mu\text{m}$ OPCPAs at 100 kHz

## Journal Article

### Author(s):

Chevreuil, Pierre-Alexis; Brunner, Fabian ; Hrisafov, Stefan; Pupeikis, Justinas; Phillips, Christopher R.; Keller, Ursula ; Gallmann, Lukas 

### Publication date:

2021-10-11

### Permanent link:

<https://doi.org/10.3929/ethz-b-000507267>

### Rights / license:

[In Copyright - Non-Commercial Use Permitted](#)

### Originally published in:

Optics Express 29(21), <https://doi.org/10.1364/oe.440273>

### Funding acknowledgement:

200416 - High repetition rate attosecond pulse generation (SNF)

# Water-window high harmonic generation with 0.8- $\mu\text{m}$ and 2.2- $\mu\text{m}$ OPCPAs at 100 kHz

P.-A. CHEVREUIL,<sup>\*</sup>  F. BRUNNER,  S. HRISAFOV,  J. PUPEIKIS,  C. R. PHILLIPS,  U. KELLER,  AND L. GALLMANN 

*Department of Physics, Institute for Quantum Electronics, ETH Zurich, Auguste-Piccard-Hof 1, 8093 Zurich, Switzerland*

*\*chpierre@phys.ethz.ch*

**Abstract:** We compare the generation of high-order harmonics in the water window (283–543 eV) with 0.8- $\mu\text{m}$  and 2.2- $\mu\text{m}$  few-cycle lasers at a pulse repetition rate of 100 kHz. Using conventional phase matching with the 2.2- $\mu\text{m}$  driver and what we attribute to nonadiabatic self-phase-matching with the 0.8- $\mu\text{m}$  driver, photons up to 0.6 keV (2 nm) are generated in both cases. Special attention is paid to the understanding of the generation mechanism with the 0.8- $\mu\text{m}$  laser amplifier system. We use the same beamline and pump laser for both drivers, which allows for a direct flux comparison at the two driving wavelengths. For photon energies around 280 eV, a 10–100 times higher flux is obtained from the 2.2- $\mu\text{m}$  versus the 0.8- $\mu\text{m}$  laser system in helium and neon. The crossover at which the 2.2- $\mu\text{m}$  yields a higher flux compared to the 0.8- $\mu\text{m}$  driver is found to be as high as 0.2 keV. Our study supports the common approach of using long-wavelength lasers in a phase-matched regime for efficient generation of water-window harmonics, but also shows that the more widespread 0.8- $\mu\text{m}$  wavelength can be used to generate water-window harmonics with an efficiency close to the one of a less common 2.2- $\mu\text{m}$  source.

© 2021 Optical Society of America under the terms of the [OSA Open Access Publishing Agreement](#)

## 1. Introduction

High harmonic generation (HHG)-based table-top extreme ultraviolet (XUV) and soft-X-ray (SXR) sources at high pulse repetition rates are becoming more and more widespread thanks to the rapid technological development of high-power solid-state lasers. Coherent SXR radiation in the biologically relevant “water window” produced by HHG in gases has received particular attention in recent years. In this spectral region spanning from 283 to 543 eV (2.3 to 4.4 nm), water is more transmissive than carbon [1,2]. The cutoff of HHG scales as  $E_{\text{cutoff}} \approx I_p + 3.17 U_p$ , with  $I_p$  the ionization potential of the gas, and  $U_p \propto I_{\text{laser}} \cdot \lambda^2$  the ponderomotive energy [3], where  $I_{\text{laser}}$  is the laser peak intensity and  $\lambda$  the laser wavelength. Thus, there are two straightforward ways for extending the cutoff energy. The first possibility consists in increasing the laser intensity for a given wavelength [4–6]. The second approach is to use a long-wavelength driver, to benefit from the quadratic scaling of the ponderomotive energy. While the microscopic response decreases with increasing wavelength [7–10], phase matching can partially compensate for this reduction [11]. Thus, most efforts in the community over the past two decades towards photon-energy scaling have been devoted to the latter approach [12–14].

Although the “intensity scaling” approach received some attention in the last few years as well [15,16], it remains less studied than the “wavelength scaling” approach due to conventional phase matching becoming impossible above  $\sim 200$  eV with a 0.8- $\mu\text{m}$  driver [17]. Several researchers aimed to overcome this phase matching challenge by using techniques such as nonadiabatic self-phase-matching (NSPM) [18–21], formation of an ion channel through electrical discharges by means of double pulses [22,23], multiple-ionizations in gases with low ionization potential gases [24], or quasi-phase-matching waveguides [25]. Several studies compared the HHG-efficiency at 0.8  $\mu\text{m}$  and at 2  $\mu\text{m}$  in a phase-matched regime at energies below 200 eV [26,27]. To our

knowledge, however, so far no study has directly compared the efficiency of unconventional phase-matching techniques with that of a long wavelength driver in a phase-matched regime.

In this paper, we experimentally compare the HHG yield in the water window driven by two state-of-the-art 100-kHz optical parametric chirped pulse amplifiers (OPCPAs) at 0.8  $\mu\text{m}$  [28] and 2.2  $\mu\text{m}$  [14]. The experiments are performed on the same beamline and both parametric sources are derived from the same pump laser to ensure comparable conditions.

## 2. HHG beyond conventional phase matching

To motivate the comparison of the two HHG approaches discussed in this work, we first examine the limitations of conventional phase matching. We then show why high intensities are needed for the 0.8- $\mu\text{m}$  driver, leading to ground-state depletion and HHG from ions. Finally, we discuss how those high intensities can be used to give rise to an unconventional phase-matching term, which can explain our HHG results with the 0.8- $\mu\text{m}$  driver.

### 2.1. Limits of conventional phase matching

While the generation of XUV/SXR in HHG happens at a single-atom level, phase matching in the macroscopic medium is required for an efficient SXR generation. Conventional phase matching of HHG is achieved through a balance of Gouy phase-shift, intensity-dependent dipole phase, dispersion from neutral atoms and dispersion from free-electrons [29]. This balance can be maintained only if the ionization level of the gas stays below the critical ionization level [11] (0.5% for helium and 1% for neon at 0.8  $\mu\text{m}$ ). This limits the intensity at which phase matching is possible, and thus the attainable cutoff. Reaching the carbon K-edge (283 eV) and oxygen K-edge (543 eV) with a 0.8- $\mu\text{m}$  driver requires intensities above  $1.4 \times 10^{15} \text{ W}\cdot\text{cm}^{-2}$  and  $2.7 \times 10^{15} \text{ W}\cdot\text{cm}^{-2}$ , respectively, which are 1.7 and 3.4 times the intensity at which the critical ionization is reached for a 2-cycle pulse in helium. To produce water-window harmonics with a 0.8- $\mu\text{m}$  driver, it is thus necessary to operate beyond the regime of conventional phase matching as Fig. 1 shows.

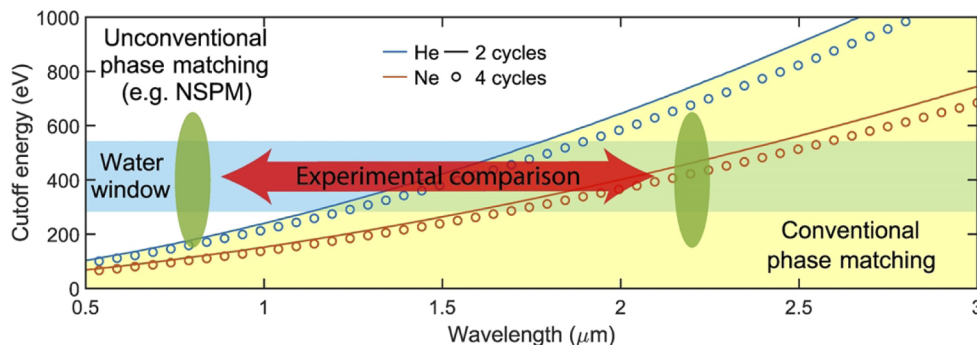


**Fig. 1.** Maximum cutoff energy which can be phase matched with conventional techniques for different parameters. We assume a carrier envelope phase (CEP) of zero. The ionization fraction is computed using the Yudin-Ivanov ionization rates [30] with the Coulomb correction factor from [31]. The yellow area represents the region in which conventional phase matching is possible. The green areas represent the two regimes we compare experimentally.

### 2.2. Changes of the atomic population at high intensities

Since conventional phase matching cannot be used to enhance HHG in the water window with a 0.8- $\mu\text{m}$  driver, it is important to understand which parameters affect the HHG yield at the microscopic level. To that end, we determine the microscopic response of the medium by

computing the nonlinear polarization  $P_{nl}$ :

$$P_{nl}(t) = N_{atom} \sum_{q=0}^{q_{max}} \eta_q(t) \cdot x_{nl}^q(t) \quad (1)$$

With  $N_{atom}$  the density of neutral atoms in the gas before interaction with the laser pulse,  $\eta_q(t)$  the proportion of atoms or ions with a charge  $q$ ,  $x_{nl}^q(t)$  the single-atom dipole moment for the species with a charge  $q$ , and  $q_{max}$  the maximum ionic charge considered. Throughout this paper, we use “single-atom dipole moment” as a short-version term for the single-atom dipole moment in the single active electron approximation for recombining trajectories only.

For simplicity, we neglect nonsequential ionization and plasma absorption. Ionization rates are computed with barrier suppression ionization (BSI)-extended ADK rates [32] (hereafter referred to as ADK-BSIe). We compute the time-dependent single-atom dipole moment acceleration [33] with a nonadiabatic Lewenstein model [29,34,35].

In Fig. 2(a), the curve showing helium with depletion attest that the generation of high-energy photons is not possible from neutral He because the ground-state is fully depleted when the field strength needed to generate such photon energies is reached. However, the depletion of the neutral helium gas population also implies that HHG from  $\text{He}^+$  becomes possible. To study at which intensities this happens, we plot in Fig. 2(b) the scaling of the microscopic spectrum in a fixed energy window. When depletion is not considered, the microscopic yield scales almost linearly with increasing intensity. However, when depletion is included, the trend changes completely, and the yield decreases with increasing intensity, as previously reported [36,37]. Including the ionization from  $\text{He}^+$  to  $\text{He}^{2+}$ , a second peak around  $10 \text{ PW}\cdot\text{cm}^{-2}$  appears, which corresponds to HHG from  $\text{He}^+$ .

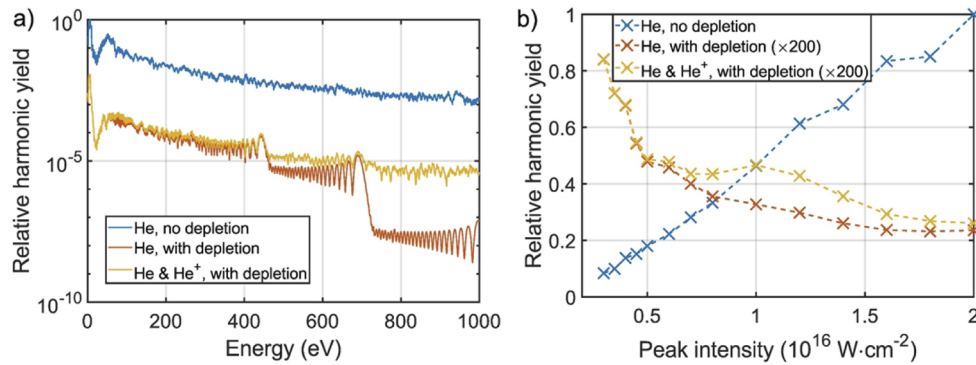


**Fig. 2.** (a) Single-atom dipole moment acceleration spectrum  $|\text{FT}[\partial_t^2 P_{nl}(t)]|^2$  (FT denoting the Fourier transform) for a 4-cycle driver at  $0.8 \mu\text{m}$  in He with a peak intensity of  $10^{16} \text{ W}\cdot\text{cm}^{-2}$ . All curves are smoothed with a 5-eV moving-average window for readability. (b) Integrated flux in a 20% bandwidth around 280 eV (252-308 eV) for the same pulse parameters as (a) with different peak intensities. The dashed lines are guides for the eye.

### 2.3. Nonadiabatic self-phase-matching

In addition to high intensities, our experiment uses few-cycle pulses. The combined presence of these two elements leads to significant population changes from one cycle to the next, as Fig. 3 shows. Such fast changes of the free-electron density leads to a strong modification of the gas refractive index on a sub-optical-cycle scale and, as a result, the laser field experiences a nonadiabatic blueshift [20,21,38,39]. This effect, named nonadiabatic self-phase-matching (NSPM), leads to a blue-shifted harmonic generation, which enhances the HHG yield [20,21].

Since it is present only when the atomic population is changing significantly during a half-cycle, few-cycle pulses and intensities in the  $10^{16}$  W·cm<sup>-2</sup> range are typically used to obtain a significant increase of the HHG yield [18,19,40]. In section 4, we show why our experimental HHG results in the water window with the 0.8- $\mu$ m driver can be explained by this effect.

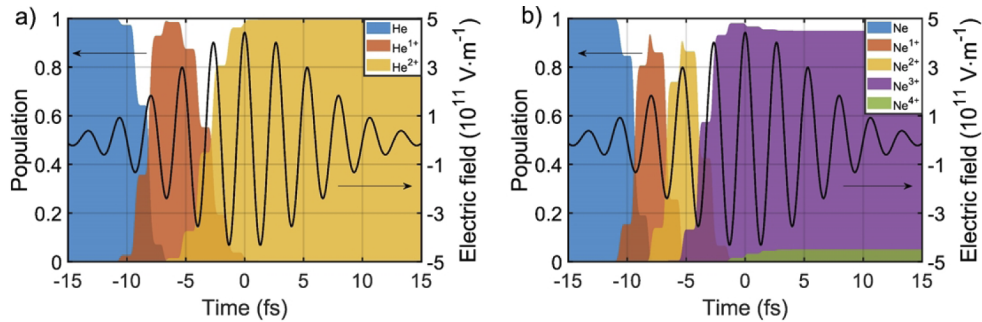


**Fig. 3.** Simulation of the evolution of ionization states for a 10-fs gaussian pulse at 0.8  $\mu$ m with a peak intensity of  $2.6 \times 10^{16}$  W·cm<sup>-2</sup> with a CEP of 0 rad in (a) helium and (b) neon. ADK-BSIe ionization rates [32] are used, non-sequential ionization and plasma absorption are neglected.

### 3. Experimental setup

#### 3.1. Laser system

Our experiment uses the output of two high-power OPCPAs operating at a 100 kHz repetition rate and sharing the same pump laser (A400, Amphos GmbH). The 0.8- $\mu$ m OPCPA produces 11-fs pulses (4 cycles) with an average power of 24 W after compression [28]. The 2.2- $\mu$ m OPCPA produces 16.5-fs pulses (2.2 cycles) with 25 W of average power [14]. In Fig. 4, we present a scheme of the experiment.

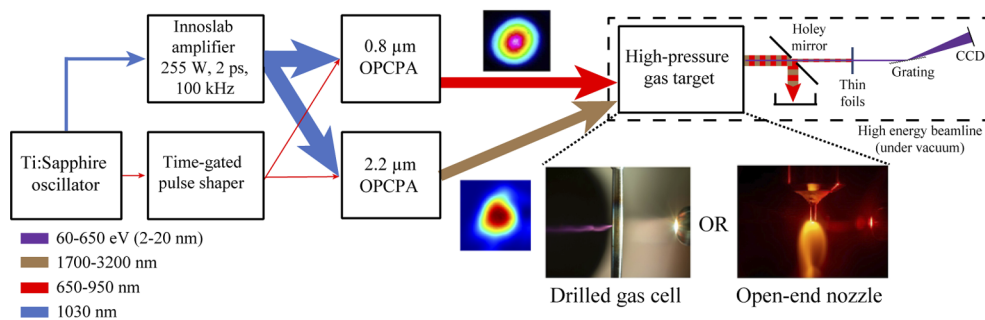


**Fig. 4.** Experimental setup. The two OPCPAs are operated one at a time.

#### 3.2. Focusing into the gas target

The 2.2- $\mu$ m beam is focused with a CaF<sub>2</sub> lens with a focal length of 75 mm. More details about our 2.2- $\mu$ m HHG experiment can be found in [14].

The 0.8- $\mu$ m beam is focused onto the HHG target at  $f/5.9$  with a silver-coated off-axis parabola ( $f=102$  mm; MDP249-P01, Thorlabs) in order to minimize optical aberrations and thus reach intensities above  $10^{16}$  W·cm<sup>-2</sup>. Great care is taken to minimize astigmatism when aligning the off-axis parabola. The off-axis parabola is water-cooled to minimize thermal lensing and

avoid thermal damage. The HHG chamber is also water-cooled due to the high thermal load. Likewise, due to the high average powers used here, the pump laser is operated all the time, and the OPCPAs are turned on 12 hours prior to the experiments for thermalization to ensure stable laser conditions during the experiments. Once the thermalized state is reached, the systems can be used for multi-day experimental campaigns without significant changes in performance.

After reflection on the off-axis parabola, the beam enters the beamline through a 5-mm thick anti-reflection (AR)-coated UV fused silica window. The window is placed as close as possible to the off-axis parabola to minimize the B-integral. To measure the beam size at the focus, we place a wedged window in the optical path and characterise the reflection from its front facet. We also add several neutral density filters for further attenuation. Hence, the beam size can be measured directly at the focus with a camera (2.2  $\mu\text{m}$  pixel size; puA1920-30um, Basler AG). We measure a  $1/e^2$ -radius beam waist of  $6 \times 7 \mu\text{m}$  at the focus and a Rayleigh length of 106  $\mu\text{m}$ , which corresponds to an estimated peak intensity of  $2.6 \times 10^{16} \text{ W}\cdot\text{cm}^{-2}$ . This is in good agreement with the theoretical values of  $3.1 \times 10^{16} \text{ W}\cdot\text{cm}^{-2}$  for the peak intensity and  $5.7 \times 5.8 \mu\text{m}$  focal spot size, computed from the incident beam profile on the off-axis parabola using Rayleigh-Sommerfeld diffraction. For the 2.2- $\mu\text{m}$  experiment, the Rayleigh lengths are estimated to be 4 mm for helium and 6 mm for neon, which are both longer than the 1-mm long gas cell.

### 3.3. Interaction geometry

After entering the beamline, the beam interacts with the gas target, which is provided either by a free-expansion nozzle with an inner diameter of 0.2 mm, or by a gas cell with 1.0-mm inner diameter and wall thickness of 0.1 mm. The gas cell approach offers the benefit of providing the same pressure in the interaction region as the backing pressure, assuming that the tube conductivity can be neglected. However, in this target geometry the gas expands into the vacuum in the beam propagation direction, leading to the accumulation of nonlinear self-effects for the laser beam before it reaches the high-pressure region. Using a supersonic expansion model [41], assuming a hole diameter of 100  $\mu\text{m}$  and a backing pressure of 1 bar, we estimate the B-integral accumulated before the gas cell entrance to be 0.1 mrad and 0.4 mrad in helium and neon respectively [42] in the generation conditions of Fig. 6. In parallel, due to the high free-electron density, plasma defocusing is also expected to occur. To estimate to what extent this may decrease the effective peak intensity, in analogy with the B-integral, we compute  $B_{\text{plasma}}$ , in which the change of refractive index is due to the free electrons. The maximum ionic state reached at a given  $z$  position is known, which allows the computation of the free-electron density. Using the same parameters as for the B-integral calculation, and assuming a cold collisionless plasma for the computation of the plasma refractive index, we estimate  $B_{\text{plasma}}$  at the gas cell entrance to be 16 mrad and 148 mrad for helium and neon, respectively. Both integrals are relatively small, thus the peak intensity in helium and neon is not expected to be greatly affected by self-effects before reaching the high-pressure zone. Experimentally, using a 1-mm drilled gas cell or a 0.2-mm open-end nozzle leads to very similar results in helium and neon, providing further evidence that self-effects before the gas cell entrance are indeed negligible.

However, part of the generated XUV/SXR will be reabsorbed in the expanding gas after interaction. Using the same gas expansion model, we find that with a backing pressure of less than 1 bar, reabsorption above 100 eV is almost negligible for hole diameters below 200  $\mu\text{m}$ : reabsorption is thus not an issue for the 0.8- $\mu\text{m}$  case where an optimal pressure is found around 380 mbar. Nonetheless, for the 2.2- $\mu\text{m}$  case, the phase-matching pressure is found to be much higher due to the low gas dispersion, resulting in an increased reabsorption. For a gas cell hole diameter of 100  $\mu\text{m}$ , we estimate an on-axis reabsorption at 300 eV of 10% at 45 bar in helium, and 46% at 12 bar in neon. It is thus necessary to stabilize the beam position efficiently once the hole is drilled to reduce unwanted enlargement of the hole resulting from beam pointing fluctuations.

In a free-expansion nozzle design, instead of the laser beam co-propagating with the expanding gas stream, the laser beam crosses the gas jet perpendicularly. This greatly decreases the effective interaction length with the target gas and hence reduces reabsorption. However, at a distance of one nozzle diameter from the tip of the nozzle, the on-axis density is 15% the density inside the nozzle [41]. Because of this rapid pressure drop as function of distance to the nozzle, this solution is not suitable for the 2.2- $\mu\text{m}$ -driven case for which pressures higher than 10 bar are required to achieve phase matching. It can, however, be used for the 0.8- $\mu\text{m}$ -driven case since optimal pressures are below 1 bar as we will see in section 4. Experimentally, we keep a distance between the bottom of the nozzle and the focus between 0.01 and 0.07 mm to minimize the pressure drop.

### 3.4. SXR filtering and detection

After interaction with the gas, most of the fundamental IR light is reflected on a holey mirror, while the XUV/SXR passes through the center hole, thanks to the different beam divergences for both wavelengths. The remaining fundamental is then filtered out by thin-metal films. For the 2.2- $\mu\text{m}$  driver, we use a single 0.1- $\mu\text{m}$  Al filter, since the fundamental light cannot be detected by the CCD of the XUV spectrometer. Furthermore, most of the generated low-energy XUV photons are reabsorbed in the supersonic expansion after interaction due to high target pressures. For the 0.8- $\mu\text{m}$ -driven HHG, we use  $2 \times 0.1\text{-}\mu\text{m}$  thick Al filters to discard the fundamental and one 0.1- $\mu\text{m}$  thick Ag filter to remove XUV light between 10 and 70 eV. One of the Al filters is placed first after HHG because we find that Al withstands the average power better than all other materials tested.

Once filtered, the harmonics are detected by an XUV/SXR spectrometer (251MX, McPherson), whose detector is a 16-bit CCD camera cooled to  $-90 \pm 5^\circ\text{C}$  (Newton 400, Andor). The spectrometer is calibrated on the absorption edges of thin films. For the 0.8- $\mu\text{m}$  case, we use the boron K-edge (188 eV), the carbon K-edge (283 eV), the titanium  $L_3$ -edge (454 eV), the oxygen K-edge (543 eV), the xenon  $M_5$ -edge (676 eV), the iron  $L_3$ -edge (707 eV) and the zinc  $L_3$ -edge (1022 eV) [1]. More details about the calibration and fundamental filtering in the 2.2- $\mu\text{m}$  case can be found in [14]. The carbon K-edge (283 eV) is visible in all measurements, and is suspected to come from organic residues in the setup. Except Fig. 6(c), all presented spectra are recorded for

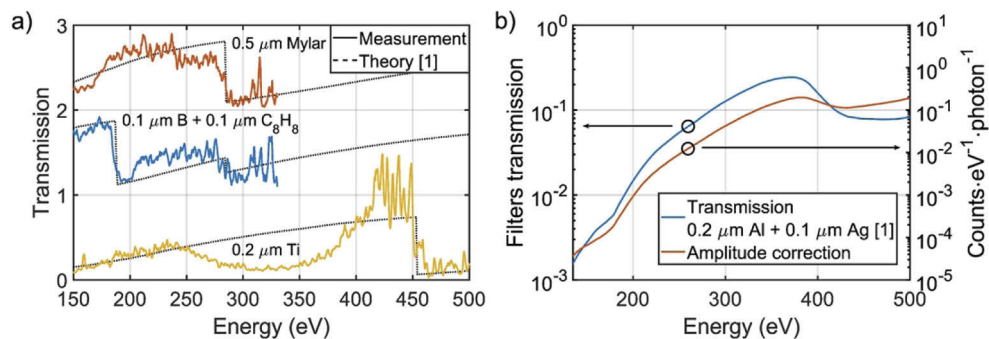


**Fig. 5.** (a) Absorption measurements of thin films using the HHG beam generated in Ne. The curves are offset by 1 with respect to each other for visibility. For the yellow curve, the measurements with and without Ti are done after Al and Ag filters. The Al and Ag filters are different (and thus have different thicknesses) in the measurement with and without Ti, explaining the “dip” around 320 eV. (b) Theoretical transmission of the filters used for all 0.8- $\mu\text{m}$  measurements (blue curve) [1], and amplitude correction curve accounting for the transmission of the same filters as the blue curve, the grating’s reflectivity, the quantum efficiency of the CCD, and the number of photons required to create one electron-hole pair.

a 1-mm wide spectrometer entrance slit and are corrected for the grating efficiency, the CCD quantum efficiency, the number of photons required to generate one electron-hole pair, the filters transmission [1] and the second diffraction order. The number of counts per photon increases with higher photon energies for all those parameters, as shown in Fig. 5(b), explaining the high dynamic range of the measurements presented below.

All spectra for the 0.8- $\mu\text{m}$  case have been recorded at least twice, to compare them and remove noise originating from cosmic rays. Stray light coming from the zero order is not expected to contribute significantly to the light detected at high photon energies, since absorption edges at high-photon energies are clearly visible as shown in Fig. 5(a). Furthermore, we find that when the Ag filter is removed, the stray light is stronger at higher photon energies (closer to grazing incidence). Therefore, if stray light was dominating the detected signal, we would detect more signal at higher photon energies compared to lower photon energies, which is not the case for any of the measurements. A 5-eV moving-average filter is applied for smoothing all spectra.

#### 4. HHG results

In this section, we focus on HHG at 0.8  $\mu\text{m}$ , since it has been less studied than phase-matched HHG at long wavelengths in the context of the generation of high-energy photons.

In Fig. 6(a) and Fig. 6(b), we present the spectra of the generated SXR as a function of the backing pressure in helium and neon, respectively. The raw spectrum without amplitude correction for HHG in helium at 380 mbar backing pressure is shown in Fig. 6(c). Harmonics are clearly visible up to 280 eV with a mean harmonic spacing of 3.42 eV, which corresponds to a fundamental wavelength blue-shifted to 725 nm ( $\Delta\omega/\omega_0 = 9\%$ ). In Fig. 6(d), we show the harmonic spacing as a function of the harmonic order, which has been computed using the position of the harmonics from Fig. 6(c).

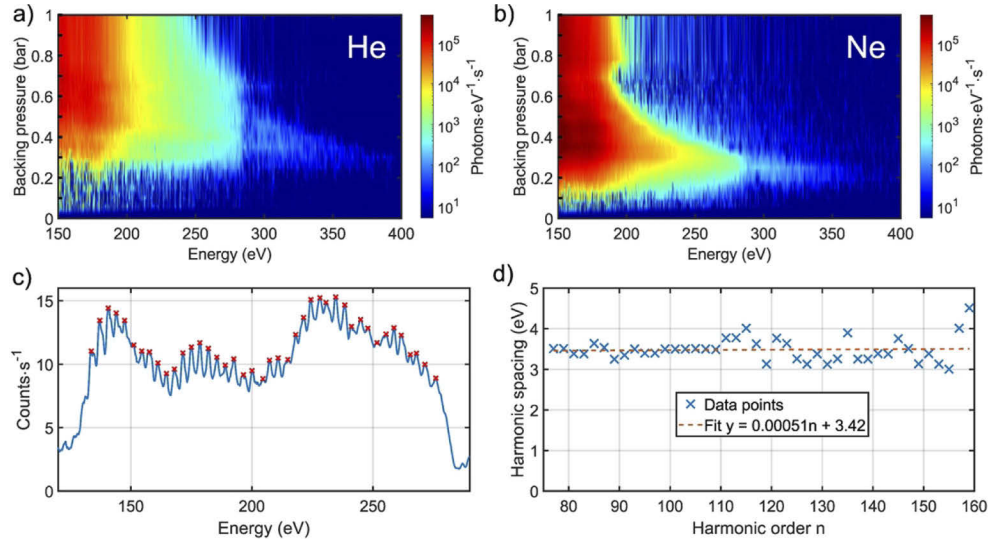


**Fig. 6.** (a-b) Pressure scans in helium and neon for HHG with the 0.8- $\mu\text{m}$  driver in a 1-mm long drilled gas cell at a peak intensity estimated to  $2.6 \times 10^{16} \text{ W}\cdot\text{cm}^{-2}$ . (c) Raw spectrum without amplitude correction for HHG in helium at 380 mbar backing pressure. The spectrometer slit is closed to 0.1 mm and the red dots indicate the local maxima. (d) Harmonic spacing as a function of harmonic order as marked by the red dots in (c). See [Data File 1](#) for underlying values.



The harmonic spacing is almost constant as a function of the harmonic order, the blueshift is therefore dominated by self-phase-modulation from 130 to 280 eV [39]. Above 280 eV, no individual harmonics are resolved, owing either to the resolution of the spectrometer at those energies (estimated to be 2-3 eV around 280 eV for a spectrometer slit aperture of 100  $\mu\text{m}$ ), or to the spectrum becoming continuous. We verify the coherence of the radiation by looking at the zero-order of the spectrometer and checking that the SXR beam is spatially confined. Uniform illumination by undirected radiation would be an indication of incoherent plasma radiation, which we do not observe.

#### 4.1. Interpretation of the 0.8- $\mu\text{m}$ -driven HHG experiment

The experimental results presented in Fig. 6 show clear optimal pressures around 300-350 mbar both in helium and in neon. One possible explanation for these optimal pressures is the presence of phase matching. A similar observation under comparable illumination conditions has already been reported in [19] and was attributed to NSPM. Indeed, our experiment reasonably fulfills both the high-intensity ( $10^{15}$ - $10^{16}$   $\text{W}\cdot\text{cm}^{-2}$ ) and the few-cycle pulse (4 cycles) requirement for NSPM, as explained in Section 2. Although shorter pulse durations are beneficial for NSPM, this effect has already been observed with similar pulse durations (12 fs at 0.8  $\mu\text{m}$  [40]).

We note that, in addition to the optimal pressure around 300 mbar, a secondary SXR flux maximum around 750 mbar is observed in neon. This “double-peak” structure has been observed on two different days (thus with slightly different laser parameters), showing that it is not an artefact from the measurement. The second peak may originate from NSPM happening at an earlier half-cycle compared to the main optimum.

To investigate whether NSPM can indeed be at the origin of our observations, we measure how the SXR spectrum evolves with increasing intensity. Tuning of the peak intensity without modifying the pulse duration and without reducing the pulse energy (e.g. by clipping the beam) is achieved by introducing astigmatism through misalignment of the off-axis parabola. In Fig. 7, our experimental results show that, at  $2\times 10^{15}$   $\text{W}\cdot\text{cm}^{-2}$  (purple curves), as expected, the spectrum decreases exponentially with increasing photon energies both in helium and in neon. Surprisingly, when the peak intensity is increased by an additional order of magnitude (yellow and orange curves in Fig. 7), the flux in the 300-600 eV region dramatically increases and a plateau emerges.

**Table 1. Summary of the parameters in the measurements shown in Fig. 7**

Gas	$I_{\text{BSI}}^{\text{a}}$ ( $\text{PW}\cdot\text{cm}^{-2}$ )	$\lambda$ ( $\mu\text{m}$ )	$N_{\text{cycles}}$	$I_{\text{peak}}$ ( $\text{PW}\cdot\text{cm}^{-2}$ )	Backing pressure <sup>d</sup> (bar)	Geometry	Interaction length (mm)	Reabsorption on-axis <sup>e</sup> (%)	$\eta_{\text{peak}}^{\text{f}}$ (%)		
He	1.5	2.2	2.2	0.42 <sup>b</sup>	45	Gas cell	1.2	10	0.02		
				2 <sup>c</sup>	74 <sup>d</sup>	Nozzle	0.2	-	40		
		0.8	4	26 <sup>e</sup>	0.48	Gas cell	1.2	0.1	100		
				26 <sup>e</sup>	70 <sup>d</sup>	Nozzle	0.2	-	100		
		Ne	0.9	2.2	2.2	0.28 <sup>b</sup>	12	Gas cell	1.2	46	0.07
						2 <sup>c</sup>	50 <sup>d</sup>	Nozzle	0.2	-	100
0.8	4			26 <sup>e</sup>	0.30	Gas cell	1.2	1.5	100		
				26 <sup>e</sup>	12 <sup>d</sup>	Nozzle	0.2	-	100		

<sup>a</sup> Barrier Suppression Ionization intensity, neglecting the Stark shift [43].

<sup>b</sup> Intensity estimated from the cutoff energy.

<sup>c</sup> Intensity estimated from a direct beam size measurement of the attenuated beam with a camera.

<sup>d</sup> The effective pressure in the interaction region is expected to be  $\sim 10$  times lower than the backing pressure.

<sup>e</sup> Estimated with the method described above at 300 eV and assuming a hole diameter of 100  $\mu\text{m}$ .

<sup>f</sup> Ionization fraction at the peak of the pulse (computed with the ADK-BSI rates for the 0.8- $\mu\text{m}$  case, and with the Yudin-Ivanov rates for the 2.2  $\mu\text{m}$  case).

This plateau, previously reported in [18], was also attributed to NSPM [20,21]. If NSPM is truly at the origin of this “plateau”, it is expected to be generated during only a few half-cycles, thus effectively producing an ionization gate [37]. This effect could therefore favour the generation of isolated attosecond pulses.

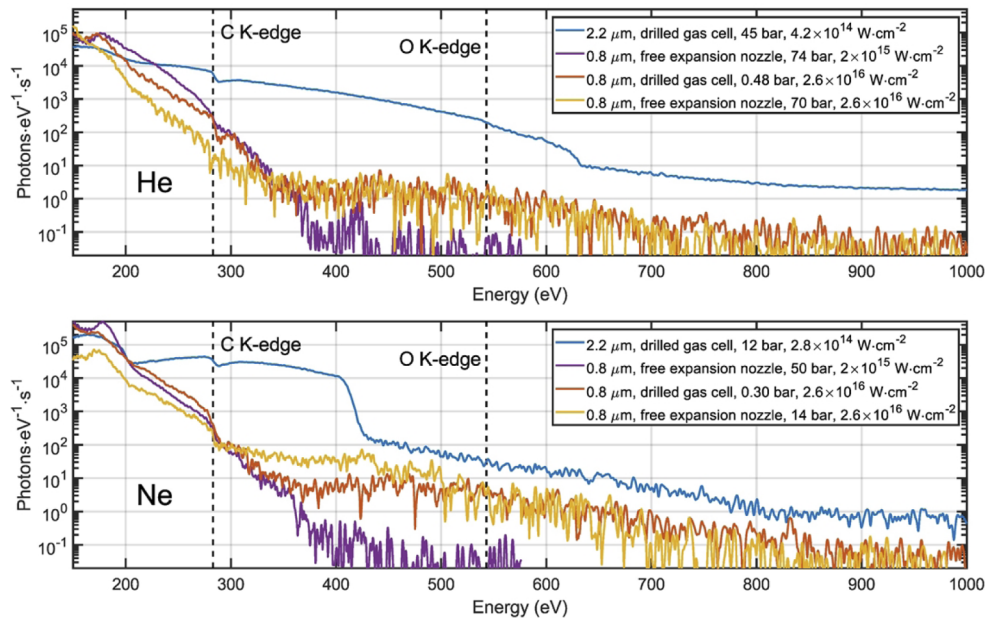


**Fig. 7.** Experimental HHG spectra with a 0.8  $\mu\text{m}$  and a 2.2  $\mu\text{m}$  driver in helium and neon. The different generation parameters are summarized in Table 1. All spectra are recorded with the same grating ( $2400\text{ g}\cdot\text{mm}^{-1}$ ), except the  $2\times 10^{15}\text{ W}\cdot\text{cm}^{-2}$  case, recorded with a  $1200\text{ g}\cdot\text{mm}^{-1}$  grating. For the latter, the diffraction efficiency above 260 eV was determined experimentally by recording the same spectrum with both gratings and using the  $2400\text{ g}\cdot\text{mm}^{-1}$  diffraction efficiency as a reference. See Data File 2 for underlying values.

#### 4.2. Comparison between 0.8 $\mu\text{m}$ and 2.2 $\mu\text{m}$ driven HHG

We now compare the 0.8- $\mu\text{m}$  and 2.2- $\mu\text{m}$  driven HHG results in Fig. 7, for which experimental parameters are summarised in Table 1 [43]. The 2.2- $\mu\text{m}$ -driven case exhibits clear cutoffs at 420 eV and 620 eV in neon and helium, respectively. Furthermore, the plateau before the observed cutoffs is an indication of phase matching in both cases.

While the absorption-limited HHG conditions are not met in the 2.2- $\mu\text{m}$  HHG experiment [14,44], the coherence length is estimated to be approximately the same or higher than the absorption length both in helium and in neon, making a direct flux comparison with the 0.8- $\mu\text{m}$  experiment meaningful both in helium and in neon. With the 0.8- $\mu\text{m}$  driver, the theoretical cutoff at  $2.6\times 10^{16}\text{ W}\cdot\text{cm}^{-2}$  is 4.9 keV, which explains why no clear cutoff can be identified in the respective spectra. The flux around the carbon K-edge (283 eV) is one to two orders of magnitude higher for the 2.2- $\mu\text{m}$  driver than for the 0.8- $\mu\text{m}$ -driven case. Around 200 eV, a crossover happens, below which the 0.8  $\mu\text{m}$  yields a higher flux than the 2.2- $\mu\text{m}$  driven source. The higher flux below 200 eV may be due to phase matching happening in the rising edge of the pulse, before the critical ionization is reached, as well as due to the stronger single-atom dipole moment at 0.8  $\mu\text{m}$  compared to 2.2  $\mu\text{m}$ . For the 0.8- $\mu\text{m}$  experiments, the decrease of the SXR flux with increasing intensity for photon energies below 300 eV may be due to a decrease of the time window during which conventional phase-matching on the rising edge of the pulse can happen.

In a 10% bandwidth around 280 eV, the IR to SXR conversion efficiency is  $3\times 10^{-13}$  and  $2\times 10^{-12}$  with the 2.2- $\mu\text{m}$  driver in helium and neon respectively, while it amounts to  $4\times 10^{-14}$  both in helium and neon with the 0.8- $\mu\text{m}$  driver.

### 4.3. Optimization of the intensity

Although few-cycle pulses and very high intensities are the prerequisite for a rapid change of the free-electron density within a half-cycle that is required by NSPM, using too high intensities results in a decrease of the nonlinear polarization because of the early ground-state depletion, as we saw in Fig. 2(a). Therefore, it is interesting to know what peak intensity optimizes this trade-off. To determine the optimum, we control the intensity with an iris placed before the off-axis parabola. The peak intensity for different iris openings is determined from a focal spot size measurement using the method described in section 3. In Fig. 8(a), we show the experimental results, in which we find two optimum intensities.

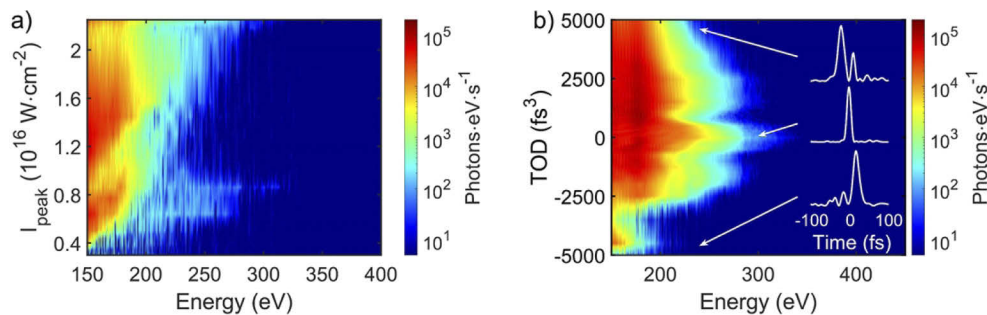


**Fig. 8.** (a) Measurement of the SXR spectrum as a function of the peak intensity in 390 mbar of helium in a 1-mm long drilled gas cell. The power is adjusted from 4 to 20 W by steps of 1 W with an iris placed before the off-axis parabola. (b) Measurement of the SXR spectrum in helium as a function of TOD with a peak intensity of  $2 \times 10^{15}$  W·cm<sup>-2</sup> with a 0.03-mm wide open-end nozzle. The 3 inserts show the driving laser temporal shape measured with frequency-resolved optical gating for three different values of TOD (-4000 fs<sup>3</sup>, 0 fs<sup>3</sup> and 4000 fs<sup>3</sup>). See [Data File 3](#) for underlying values.

The first one around  $0.8 \times 10^{16}$  W·cm<sup>-2</sup> may be due to HHG emission from He<sup>+</sup>, since emission from this ion is expected to happen around  $10^{16}$  W·cm<sup>-2</sup>, as shown in Fig. 2(a). The observation of a second “optimum” intensity around  $2.3 \times 10^{16}$  W·cm<sup>-2</sup> (maximum peak intensity achievable within our experimental conditions) cannot be expected from the nonlinear simulation shown in Fig. 2(b): in fact, the nonlinear polarization is expected to keep decreasing above  $1-1.5 \times 10^{16}$  W·cm<sup>-2</sup> because of the depletion of He<sup>+</sup>. This can, however, be explained when taking the effect of NSPM into account: higher peak intensities lead to larger transient changes of the He and He<sup>+</sup> population within a half-cycle, leading to more effective NSPM, and thus higher flux. The flux generated is then not expected to originate from the most intense parts of the pulse, but rather from its rising edge, between 5 to 10 fs before the peak of the pulse.

### 4.4. Optimization of the pulse shape

Since generating HHG at such high photon energies requires to maintain as much of the population in the ground-state before the peak of the pulse as possible, pre-pulses have to be avoided as they deplete part of the ground-state without contributing to the HHG at high photon energies.

However, one of the most common ways to obtain few-cycle pulses is to post-compress long pulses in rare gases, which generally creates a large temporal pedestal and pre-pulses. To study the suitability of such sources as HHG drivers in this high-intensity regime, we start from close to Fourier-limited pulses, and add third-order dispersion (TOD) with our time-gated pulse shaper [45] to control the appearance and strength of pre-pulses. Such a scan is shown in Fig. 8(b). Within the range of applied TOD, the impact of the pulse shaping on the OPCPA power and spectrum is negligible.

As can be seen in Fig. 8(b), the yield is strongly asymmetric with respect to TOD: a negative TOD (pre-pulse) yields a much lower flux than the same amount of positive TOD (post-pulse). This shows that driving high-photon energy HHG at high intensities is much more efficient when the rising edge of the pulse is very “clean”, which is more challenging to attain with post-compressed sources. We note, however, that most of the previous demonstrations of NSPM used such post-compressed sources to benefit from the shorter pulse durations. Further investigation is required to determine the optimum in this trade-off between shorter post-compressed pulses and longer, but cleaner pulses with little or no post-compression.

## 5. Conclusion

We explored the generation of high-order harmonics in the water window with two few-cycle sources at 0.8  $\mu\text{m}$  and 2.2  $\mu\text{m}$  center wavelength and 100 kHz repetition rate. With both sources, we obtain HHG spanning the full water window up to 0.6 keV. The HHG at 0.8  $\mu\text{m}$  in helium and neon represents what is, to our knowledge, the first demonstration of water-window harmonics at 100 kHz repetition rate for this driving wavelength. The generation of photons in the 300-600 eV range is attributed to NSPM. We show that a clean temporal trace is necessary to efficiently generate harmonics in this unconventional phase-matching regime, to reduce early depletion of the ground-state. When comparing the flux of the 0.8- $\mu\text{m}$  driven source in helium and neon with the 2.2- $\mu\text{m}$  driven one, we find that 200 eV represents a crossover point above which the 2.2- $\mu\text{m}$  source yields a higher flux compared to 0.8  $\mu\text{m}$ . Around the carbon K-edge (283 eV), the 2.2- $\mu\text{m}$ -driven source produces a flux between 10 and 100 times higher than the 0.8- $\mu\text{m}$ -driven one. Our experiments confirm the current approach in the attosecond community of using long-wavelength lasers in a phase-matched regime rather than short-wavelength lasers in a transiently phase-matched regime for efficient generation of harmonics in the water window.

**Funding.** Schweizerischer Nationalfonds zur Förderung der Wissenschaftlichen Forschung (200020\_200416); FAST initiative of NCCR MUST.

**Acknowledgments.** We acknowledge Anne L’Huillier, Cord Arnold and Chen Guo for fruitful discussions. We also thank Marcel Baer and Andreas Stuker with his team for the free-expansion nozzle design and manufacturing.

**Disclosures.** The authors declare no conflicts of interest.

**Data availability.** The data underlying the results presented in this paper are publicly available in [46].

## References

1. B. L. Henke, E. M. Gullikson, and J. C. Davis, “X-Ray Interactions: Photoabsorption, Scattering, Transmission, and Reflection at  $E = 50\text{--}30,000$  eV,  $Z = 1\text{--}92$ ,” *At. Data Nucl. Data Tables* **54**(2), 181–342 (1993).
2. C. Kleine, M. Ekimova, G. Goldsztejn, S. Raabe, C. Strüber, J. Ludwig, S. Yarlagadda, S. Eisebitt, M. J. J. Vrakking, T. Elsaesser, E. T. J. Nibbering, and A. Rouzée, “Soft X-ray Absorption Spectroscopy of Aqueous Solutions Using a Table-Top Femtosecond Soft X-ray Source,” *J. Phys. Chem. Lett.* **10**(1), 52–58 (2019).
3. J. L. Krause, K. J. Schafer, and K. C. Kulander, “High-order harmonic generation from atoms and ions in the high intensity regime,” *Phys. Rev. Lett.* **68**(24), 3535–3538 (1992).
4. C. Spielmann, N. H. Burnett, S. Sartania, R. Koppitsch, M. Schnürer, C. Kan, M. Lenzner, P. Wobruschek, and F. Krausz, “Generation of Coherent X-rays in the Water Window Using 5-Femtosecond Laser Pulses,” *Science* **278**(5338), 661–664 (1997).
5. Z. Chang, A. Rundquist, H. Wang, M. M. Murnane, and H. C. Kapteyn, “Generation of Coherent Soft X Rays at 2.7 nm Using High Harmonics,” *Phys. Rev. Lett.* **79**(16), 2967–2970 (1997).
6. M. Schnürer, C. Spielmann, P. Wobruschek, C. Strelt, N. H. Burnett, C. Kan, K. Ferencz, R. Koppitsch, Z. Cheng, T. Brabec, and F. Krausz, “Coherent 0.5-keV X-Ray Emission from Helium Driven by a Sub-10-fs Laser,” *Phys. Rev. Lett.* **80**(15), 3236–3239 (1998).
7. J. Tate, T. Augustine, H. G. Muller, P. Salières, P. Agostini, and L. F. DiMauro, “Scaling of Wave-Packet Dynamics in an Intense Midinfrared Field,” *Phys. Rev. Lett.* **98**(1), 013901 (2007).
8. K. Schiessl, K. L. Ishikawa, E. Persson, and J. Burgdörfer, “Quantum Path Interference in the Wavelength Dependence of High-Harmonic Generation,” *Phys. Rev. Lett.* **99**(25), 253903 (2007).
9. M. V. Frolov, N. L. Manakov, and A. F. Starace, “Wavelength Scaling of High-Harmonic Yield: Threshold Phenomena and Bound State Symmetry Dependence,” *Phys. Rev. Lett.* **100**(17), 173001 (2008).

10. C.-J. Lai, G. Cirmi, K.-H. Hong, J. Moses, S.-W. Huang, E. Granados, P. Keathley, S. Bhardwaj, and F. X. Kärtner, "Wavelength Scaling of High Harmonic Generation Close to the Multiphoton Ionization Regime," *Phys. Rev. Lett.* **111**(7), 073901 (2013).
11. T. Popmintchev, M.-C. Chen, A. Bahabad, M. Gerrity, P. Sidorenko, O. Cohen, I. P. Christov, M. M. Murnane, and H. C. Kapteyn, "Phase matching of high harmonic generation in the soft and hard X-ray regions of the spectrum," *Proc. Natl. Acad. Sci.* **106**(26), 10516–10521 (2009).
12. T. Popmintchev, M.-C. Chen, D. Popmintchev, P. Arpin, S. Brown, S. Alisauskas, G. Andriukaitis, T. Balciunas, O. D. Mucke, A. Pugzlys, A. Baltuska, B. Shim, S. E. Schrauth, A. Gaeta, C. Hernandez-Garcia, L. Plaja, A. Becker, A. Jaron-Becker, M. M. Murnane, and H. C. Kapteyn, "Bright Coherent Ultrahigh Harmonics in the keV X-ray Regime from Mid-Infrared Femtosecond Lasers," *Science* **336**(6086), 1287–1291 (2012).
13. E. J. Takahashi, T. Kanai, K. L. Ishikawa, Y. Nabekawa, and K. Midorikawa, "Coherent Water Window X Ray by Phase-Matched High-Order Harmonic Generation in Neutral Media," *Phys. Rev. Lett.* **101**(25), 253901 (2008).
14. J. Pupeikis, P.-A. Chevreauil, N. Bigler, L. Gallmann, C. R. Phillips, and U. Keller, "Water window soft x-ray source enabled by a 25 W few-cycle 2.2  $\mu\text{m}$  OPCPA at 100 kHz," *Optica* **7**(2), 168–171 (2020).
15. N. Ishii, S. Adachi, Y. Nomura, A. Kosuge, Y. Kobayashi, T. Kanai, J. Itatani, and S. Watanabe, "Generation of soft x-ray and water window harmonics using a few-cycle, phase-locked, optical parametric chirped-pulse amplifier," *Opt. Lett.* **37**(1), 97–99 (2012).
16. J. Rothhardt, S. Hädrich, A. Klenke, S. Demmler, A. Hoffmann, T. Gotschall, T. Eidam, M. Krebs, J. Limpert, and A. Tünnermann, "53 W average power few-cycle fiber laser system generating soft x rays up to the water window," *Opt. Lett.* **39**(17), 5224–5227 (2014).
17. T. Popmintchev, M.-C. Chen, O. Cohen, M. E. Grisham, J. J. Rocca, M. M. Murnane, and H. C. Kapteyn, "Extended phase matching of high harmonics driven by mid-infrared light," *Opt. Lett.* **33**(18), 2128–2130 (2008).
18. E. Seres, J. Seres, F. Krausz, and C. Spielmann, "Generation of Coherent Soft-X-Ray Radiation Extending Far Beyond the Titanium L Edge," *Phys. Rev. Lett.* **92**(16), 163002 (2004).
19. J. Seres, P. Wobrauschek, C. Strelt, V. S. Yakovlev, E. Seres, F. Krausz, and C. Spielmann, "Generation of coherent keV x-rays with intense femtosecond laser pulses," *New J. Phys.* **8**(10), 251–254 (2006).
20. M. Geissler, G. Tempea, and T. Brabec, "Phase-matched high-order harmonic generation in the nonadiabatic limit," *Phys. Rev. A* **62**(3), 033817 (2000).
21. G. Tempea, M. Geissler, M. Schnürer, and T. Brabec, "Self-Phase-Matched High Harmonic Generation," *Phys. Rev. Lett.* **84**(19), 4329–4332 (2000).
22. J. Seres, E. Seres, and C. Spielmann, "Monitoring the He<sup>+</sup> ion channel formation by high-order harmonic generation," *Opt. Express* **17**(3), 1493–1501 (2009).
23. J. Seres, E. Seres, B. Landgraf, B. Aurand, T. Kuehl, and C. Spielmann, "Quantum Path Interference and Multiple Electron Scattering in Soft X-Ray High-Order Harmonic Generation," *Photonics* **2**(1), 104–123 (2015).
24. P. Arpin, T. Popmintchev, N. L. Wagner, A. L. Lytle, O. Cohen, H. C. Kapteyn, and M. M. Murnane, "Enhanced High Harmonic Generation from Multiply Ionized Argon above 500 eV through Laser Pulse Self-Compression," *Phys. Rev. Lett.* **103**(14), 143901 (2009).
25. E. A. Gibson, A. Paul, N. Wagner, R. Tobey, D. Gaudiosi, S. Backus, I. P. Christov, A. Aquila, E. M. Gullikson, D. T. Attwood, M. M. Murnane, and H. C. Kapteyn, "Coherent Soft X-ray Generation in the Water Window with Quasi-Phase Matching," *Science* **302**(5642), 95–98 (2003).
26. M.-C. Chen, C. Mancuso, C. Hernandez-Garcia, F. Dollar, B. Galloway, D. Popmintchev, P.-C. Huang, B. Walker, L. Plaja, A. A. Jaro -Becker, A. Becker, M. M. Murnane, H. C. Kapteyn, and T. Popmintchev, "Generation of bright isolated attosecond soft X-ray pulses driven by multicycle midinfrared lasers," *Proc. Natl. Acad. Sci.* **111**(23), E2361–E2367 (2014).
27. B. Li, K. Wang, X. Tang, Y. Chen, C. D. Lin, and C. Jin, "Generation of isolated soft x-ray attosecond pulses with mid-infrared driving lasers via transient phase-matching gating," *New J. Phys.* **23**(7), 073051 (2021).
28. S. Hrisafov, J. Pupeikis, P.-A. Chevreauil, F. Brunner, C. R. Phillips, L. Gallmann, and U. Keller, "High-power few-cycle near-infrared OPCPA for soft X-ray generation at 100 kHz," *Opt. Express* **28**(26), 40145–40154 (2020).
29. M. B. Gaarde, J. L. Tate, and K. J. Schafer, "Macroscopic aspects of attosecond pulse generation," *J. Phys. B: At., Mol. Opt. Phys.* **41**(13), 132001 (2008).
30. G. L. Yudin and M. Y. Ivanov, "Nonadiabatic tunnel ionization: Looking inside a laser cycle," *Phys. Rev. A* **64**(1), 013409 (2001).
31. S. V. Popruzhenko, V. D. Mur, V. S. Popov, and D. Bauer, "Strong Field Ionization Rate for Arbitrary Laser Frequencies," *Phys. Rev. Lett.* **101**(19), 193003 (2008).
32. V. P. Krainov, "Ionization rates and energy and angular distributions at the barrier-suppression ionization of complex atoms and atomic ions," *J. Opt. Soc. Am. B* **14**(2), 425–431 (1997).
33. K. Burnett, V. C. Reed, J. Cooper, and P. L. Knight, "Calculation of the background emitted during high-harmonic generation," *Phys. Rev. A* **45**(5), 3347–3349 (1992).
34. M. Lewenstein, P. Balcou, M. Y. Ivanov, A. L'Huillier, and P. B. Corkum, "Theory of high-harmonic generation by low-frequency laser fields," *Phys. Rev. A* **49**(3), 2117–2132 (1994).
35. E. Priori, G. Cerullo, M. Nisoli, S. Stagira, S. De Silvestri, P. Villoresi, L. Poletto, P. Ceccherini, C. Altucci, R. Bruzese, and C. de Lisio, "Nonadiabatic three-dimensional model of high-order harmonic generation in the few-optical-cycle regime," *Phys. Rev. A* **61**(6), 063801 (2000).

36. A. Gordon and F. X. Kartner, "Scaling of keV HHG photon yield with drive wavelength," *Opt. Express* **13**(8), 2941–2947 (2005).
37. V. V. Strelkov, A. F. Sterjantov, N. Y. Shubin, and V. T. Platonenko, "XUV generation with several-cycle laser pulse in barrier-suppression regime," *J. Phys. B: At., Mol. Opt. Phys.* **39**(3), 577–589 (2006).
38. C. Altucci, R. Bruzzese, C. de Lisio, M. Nisoli, S. Stagira, S. De Silvestri, O. Svelto, A. Boscolo, P. Ceccherini, L. Poletto, G. Tondello, and P. Villorosi, "Tunable soft-x-ray radiation by high-order harmonic generation," *Phys. Rev. A* **61**(2), 021801 (1999).
39. H. J. Shin, D. G. Lee, Y. H. Cha, K. H. Hong, and C. H. Nam, "Generation of Nonadiabatic Blueshift of High Harmonics in an Intense Femtosecond Laser Field," *Phys. Rev. Lett.* **83**(13), 2544–2547 (1999).
40. E. Seres, J. Seres, and C. Spielmann, "X-ray absorption spectroscopy in the keV range with laser generated high harmonic radiation," *Appl. Phys. Lett.* **89**(18), 181919 (2006).
41. D. R. Miller, "Free Jet Sources," in *Atomic and Molecular Beam Methods* (G. Scoles, Oxford University, 1988), pp. 14–53.
42. C. Bree, A. Demircan, and G. Steinmeyer, "Method for Computing the Nonlinear Refractive Index via Keldysh Theory," *IEEE J. Quantum Electron.* **46**(4), 433–437 (2010).
43. F. A. Ilkov, J. E. Decker, and S. L. Chin, "Ionization of atoms in the tunnelling regime with experimental evidence using Hg atoms," *J. Phys. B: At., Mol. Opt. Phys.* **25**(19), 4005–4020 (1992).
44. E. Constant, D. Garzella, P. Breger, E. Mével, C. Dorrer, C. Le Blanc, F. Salin, and P. Agostini, "Optimizing High Harmonic Generation in Absorbing Gases: Model and Experiment," *Phys. Rev. Lett.* **82**(8), 1668–1671 (1999).
45. J. Pupeikis, N. Bigler, S. Hrisafov, C. R. Phillips, and U. Keller, "Programmable pulse shaping for time-gated amplifiers," *Opt. Express* **27**(1), 175 (2019).
46. P.-A. Chevreuril, F. Brunner, J. Pupeikis, C. R. Phillips, U. Keller, and L. Gallmann, "Supplementary document for Water-window high harmonic generation with 0.8- $\mu\text{m}$  and 2.2- $\mu\text{m}$  OPCAs at 100 kHz," (2021).